

Supporting Information

S1. Typical parameters of Ge₂Sb₂Te₅.

Table S1. Typical parameters of Ge₂Sb₂Te₅.

Parameters	Value	Ref.
r	0.1365 nm	[1]
R_h	0.1365 nm	[1]
λ_j	0.299 nm	[2]
ΔH_f	$625 \times 10^6 \text{ J/m}^3$	[2]
v_m	$2.9 \times 10^{-28} \text{ m}^3$	[2]
T_m	900 K	[2]
σ	0.06 J/m^2	[3]
E_a	2.45 eV	[4]
η_∞	0.012 Pa s	[1]
T_g	472 K	[1]
m	140	[1]
T_{glass}	534 K	[1]
θ	130°	[2]
n_a+ik_a	4.36-1.79i	[5]
n_c+ik_c	4.61-4.01i	[5]

The optical constants in last two lines correspond to the optical wavelength of 660 nm.

S2. Viscosity model.

Recent study verified that the viscosity of phase-change materials conforms to different models at different temperature range. In the supercooled liquid state ($T \geq T_{glass}$), the viscosity is given by the Mauro-Yue-Ellison-Gupta-Allan (MYEGA) model [6] as

$$\log_{10} \eta = \log_{10} \eta_\infty + (12 - \log_{10} \eta_\infty) \frac{T_g}{T} \exp \left[\left(\frac{m}{12 - \log_{10} \eta_\infty} - 1 \right) \left(\frac{T_g}{T} - 1 \right) \right] \quad (S1)$$

where, η_∞ is the viscosity extrapolated to infinite temperature, m is the fragility, and T_g is the temperature at which the viscosity is equal to $10^{12} \text{ Pa}\cdot\text{s}$.

In the glass state ($T < T_{glass}$), the viscosity is given by the Arrhenius model as

$$\eta = \eta_0 \exp\left(\frac{E_a}{k_B T}\right) \quad (S2)$$

where, η_0 is a prefactor to equal Eq. (S1) and (S2) at T_{glass} .

Using typical parameters of $\text{Ge}_2\text{Sb}_2\text{Te}_5$ in Table S1, the viscosity of $\text{Ge}_2\text{Sb}_2\text{Te}_5$ as a function of temperature is shown in Figure S1.

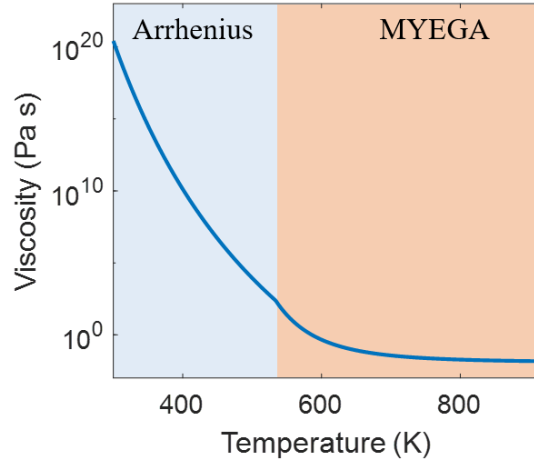


Figure S1. The piecewise viscosity model of $\text{Ge}_2\text{Sb}_2\text{Te}_5$.

S3. Probabilities of nucleation, growth and dissociation.

Using Eq. (4-6) and typical parameters of $\text{Ge}_2\text{Sb}_2\text{Te}_5$ in Table S1, the probabilities of nucleation, growth and dissociation are calculated at different temperatures, shown in Figure S2. From it, the growth probability is much larger than the nucleation probability at high temperature. In addition, the dissociation probability becomes larger than the grow probability for temperature $> 788\text{K}$.

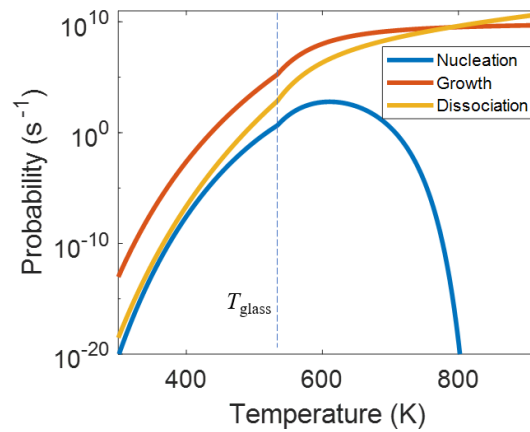


Figure S2. Probabilities of nucleation, growth and dissociation at different temperatures.

S4. Non-uniform meshing technique

Here, we take a one-dimensional (1D) heat transfer scene as an example to illustrate how to solve the heat conduction equation by exploiting the non-uniform meshing technique. Figure S3(a) shows a 1D object and its three adjacent grid points with arbitrary distance of Δx_{i-1} and Δx_i . Its temperature profile is simulated by a 1D heat conduction equation,

$$\rho c \frac{\partial T(x, t)}{\partial t} = k \nabla^2 T(x, t) + Q(x, t) \quad (\text{S3})$$

Using the central difference method to convert the derivative to the difference, the equation (S3) becomes

$$T_i^{l+1} = T_i^l + \frac{k \Delta t}{\rho c} \frac{2 \left[\Delta x_{i-1} (T_{i+1}^l - T_i^l) - \Delta x_i (T_i^l - T_{i-1}^l) \right]}{\Delta x_i \Delta x_{i-1} (\Delta x_i + \Delta x_{i-1})} + \frac{\Delta t}{\rho c} Q_i^l. \quad (\text{S4})$$

where, T_i^l and T_i^{l+1} are the temperatures at the present and next moments.

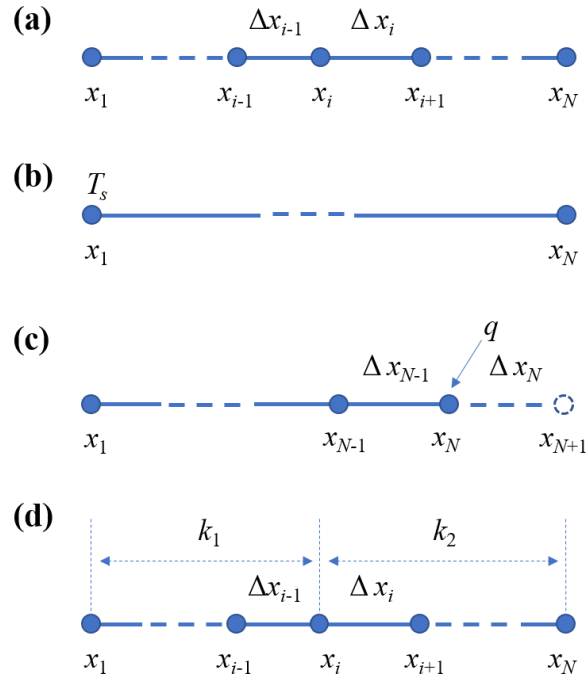


Figure S3. Schematic diagram of 1D heat transfer scene with non-uniform grid. (a) A 1D object and three adjacent grid points. (b) Dirichlet boundary condition. (c) Neumann boundary condition. (d) Interface boundary condition.

The boundary conditions can be dealt with as follows:

(1) Dirichlet boundary condition: A boundary has a specified temperature. For example, if the temperature at boundary x_1 is always equal to T_s (Figure S3(b)), we can get $T_1^{l+1} \equiv T_s$.

(2) Neumann boundary condition: A boundary has a specified heat flux. For example, if there is a heat flux q at boundary x_N (Figure S3(c)), according to Fourier's law, we can get

$$-k \frac{\partial T(x, t)}{\partial x} \Big|_{x_N} = q. \text{ Converting to the difference scheme, it becomes } -k \frac{T_{N+1}^l - T_{N-1}^l}{\Delta x_N + \Delta x_{N-1}} = q. \text{ As}$$

x_{N+1} and Δx_N are located outside the object, we can get $T_{N+1}^l = T_{N-1}^l - \frac{2\Delta x_{N-1}}{k} q$ by assuming

$\Delta x_N = \Delta x_{N-1}$. Then, the equation (S4) becomes

$$T_N^{l+1} = T_N^l + \frac{2k\Delta t}{\rho c} \frac{T_{N-1}^l - T_N^l}{\Delta x_{N-1}^2} - \frac{2\Delta t}{\rho c \Delta x_{N-1}} q + \frac{\Delta t}{\rho c} Q_N^l. \quad (\text{S5})$$

Insulated boundary condition: A boundary has zero heat flux. If there is no heat flux at boundary x_N , i.e., $q = 0$, the equation (S4) becomes

$$T_N^{l+1} = T_N^l + \frac{2k\Delta t}{\rho c} \frac{T_{N-1}^l - T_N^l}{\Delta x_{N-1}^2} + \frac{\Delta t}{\rho c} Q_N^l. \quad (\text{S6})$$

(3) Interface boundary condition: Two objects with different heat conduction coefficients contact with each other at a boundary. For example, if two objects with heat conduction coefficients of k_1 and k_2 perfectly contact at grid point x_i (Figure S3(d)), we have

$$\begin{cases} T(x, t) \Big|_{x_i^-} = T(x, t) \Big|_{x_i^+} \\ -k_1 \frac{\partial T(x, t)}{\partial x} \Big|_{x_i^-} = -k_2 \frac{\partial T(x, t)}{\partial x} \Big|_{x_i^+} \end{cases}. \quad (\text{S7})$$

Converting to the difference scheme, we can obtain

$$T_i^{l+1} = \frac{k_2 \Delta x_{i-1} T_{i+1}^l + k_1 \Delta x_i T_i^l}{k_2 \Delta x_{i-1} + k_1 \Delta x_i}. \quad (\text{S8})$$

S5. A time-step alternation strategy

In explicit finite difference method, based on the stability requirements, the maximum time step is

$$\Delta t_{\max} = \frac{\rho c h^2}{6k}, \quad (\text{S9})$$

where, ρ is the density, c is the specific heat capacity, k is the heat conduction coefficient, h is the space step. If using the non-uniform mesh, h is the minimum space step. Hence, the smaller the space step is, the smaller the time step is and the longer the calculation time is.

If multiple time steps are alternately exploited in calculation, the average time step will be larger than Δt_{\max} . Taking two time steps as an example, the optimal time steps should be

$$\begin{aligned} \Delta t_1 &= 2\left(1 + \sqrt{2}/2\right)\Delta t_{\max} \\ \Delta t_2 &= 2\left(1 - \sqrt{2}/2\right)\Delta t_{\max} \end{aligned} \quad (\text{S10})$$

Then, the average time step is twice as much as Δt_{\max} .

S6. Variation rate of peak temperature

To better understand the ultrafast change of peak temperature at 3.0 mW, its variation rate is given by computing the derivative, shown in Figure S4. Obviously, at the moments that the laser is turned on and off, the heating rate and quenching rate can reach to 1.7×10^{10} K/s and -2.4×10^{10} K/s, respectively. From Figure S4(b), the variation rate of the peak temperature becomes slightly higher at 110 ns, which is due to the higher single-pass absorption of the crystallized film in comparison to the amorphous background.

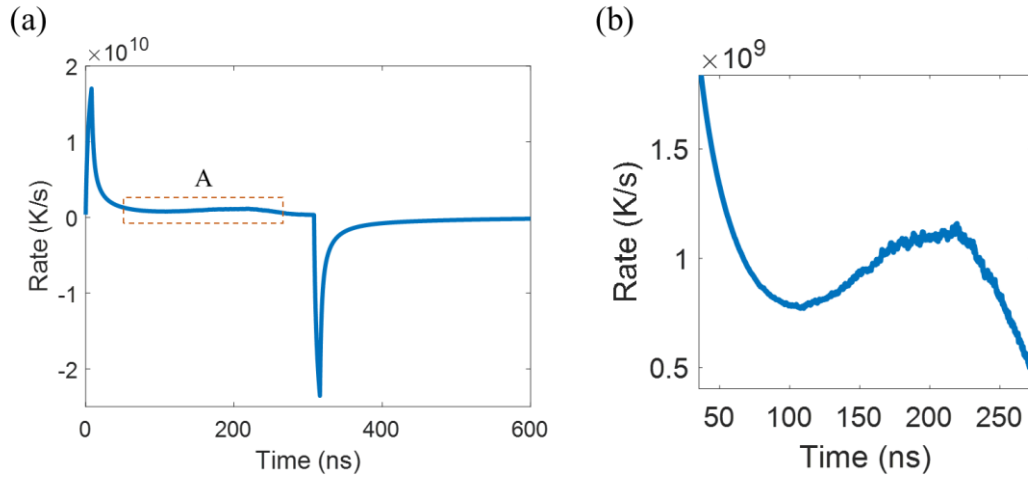


Figure S4. (a) Variation rate of peak temperature at 3.0 mW. (b) The zoom-in view of section A in (a).

S7. Transient evolution of peak temperature.

Figure S5 shows the transient evolution of the peak temperature for 300 ns laser pulses with powers varying from 0 to 5.0 mW.

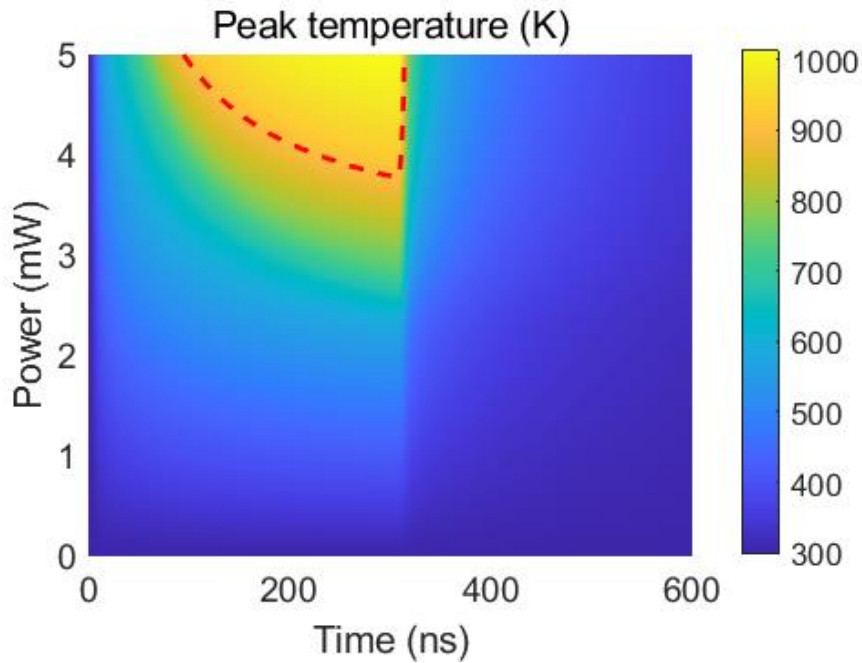


Figure S5. Transient evolution of peak temperature at different laser power. The red dashed line represents the melting temperature of 900 K.

S8. Crystallisation process at 5.0 mW.

Figure S6 shows the crystallisation kinetics at 5.0 mW and some snapshots of crystal structures. Crystallisation starts at 35 ns, and then the crystallised region is expanding (see (i-iii) in Figure S6c). At ~ 95 ns, the temperature reaches to the melting temperature, at which the center of the crystallised region begins melting. The melting area becomes larger and larger until the laser pulse ends (see (iv-v)). Once the laser pulse ends, the temperature quickly declines below the melting temperature, and re-crystallisation happens (see (vi-vii)). Finally, the melting region totally becomes crystalline phase due to the large growth velocity of $\text{Ge}_2\text{Sb}_2\text{Te}_5$ and pre-existing crystalline surroundings. Therefore, the re-crystallisation regions have the same crystal orientations with the surrounding grains, making that the grain sizes at the center are much larger than those at the boundary (see (viii)). The evolution of the microstructure is best seen using Movie 2 in SI.

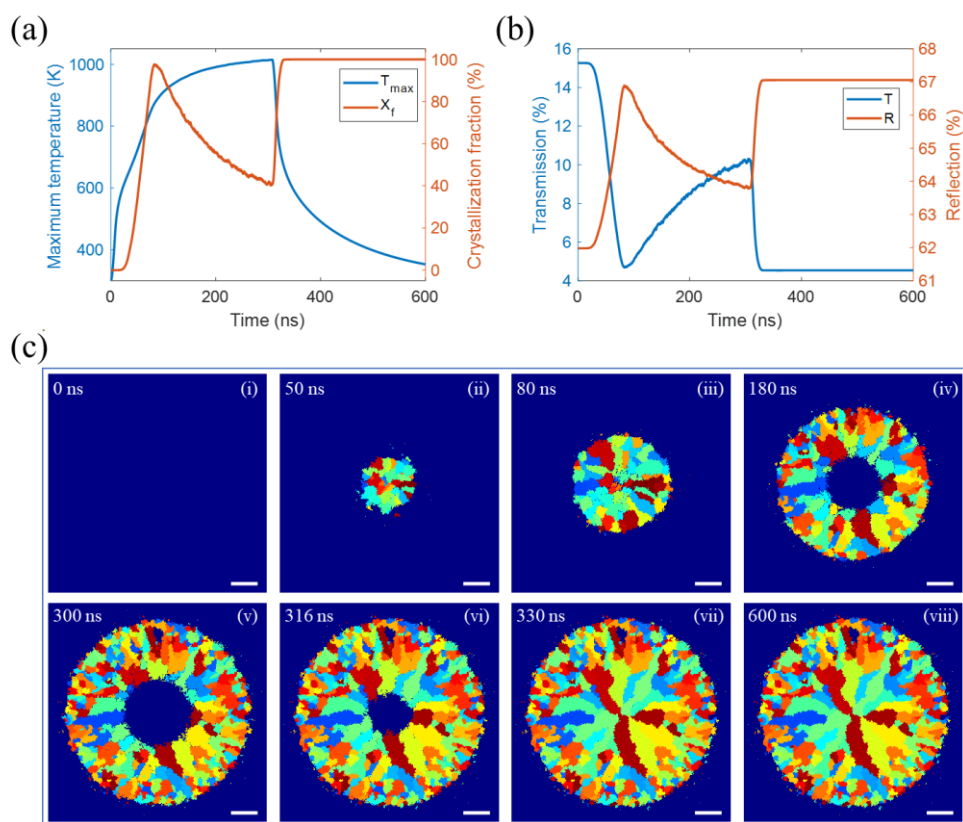


Figure S6. Laser-induced crystallisation at 5.0 mW. (a) The maximum temperature (T_{\max}) and crystallisation fraction (X_f) versus time. (b) The transmission (T) and reflection (R) versus

time. (c) The crystallographic structures of $\text{Ge}_2\text{Sb}_2\text{Te}_5$ film at different time. Scale bar is 200 nm.

S9. Crystallisation at different laser widths

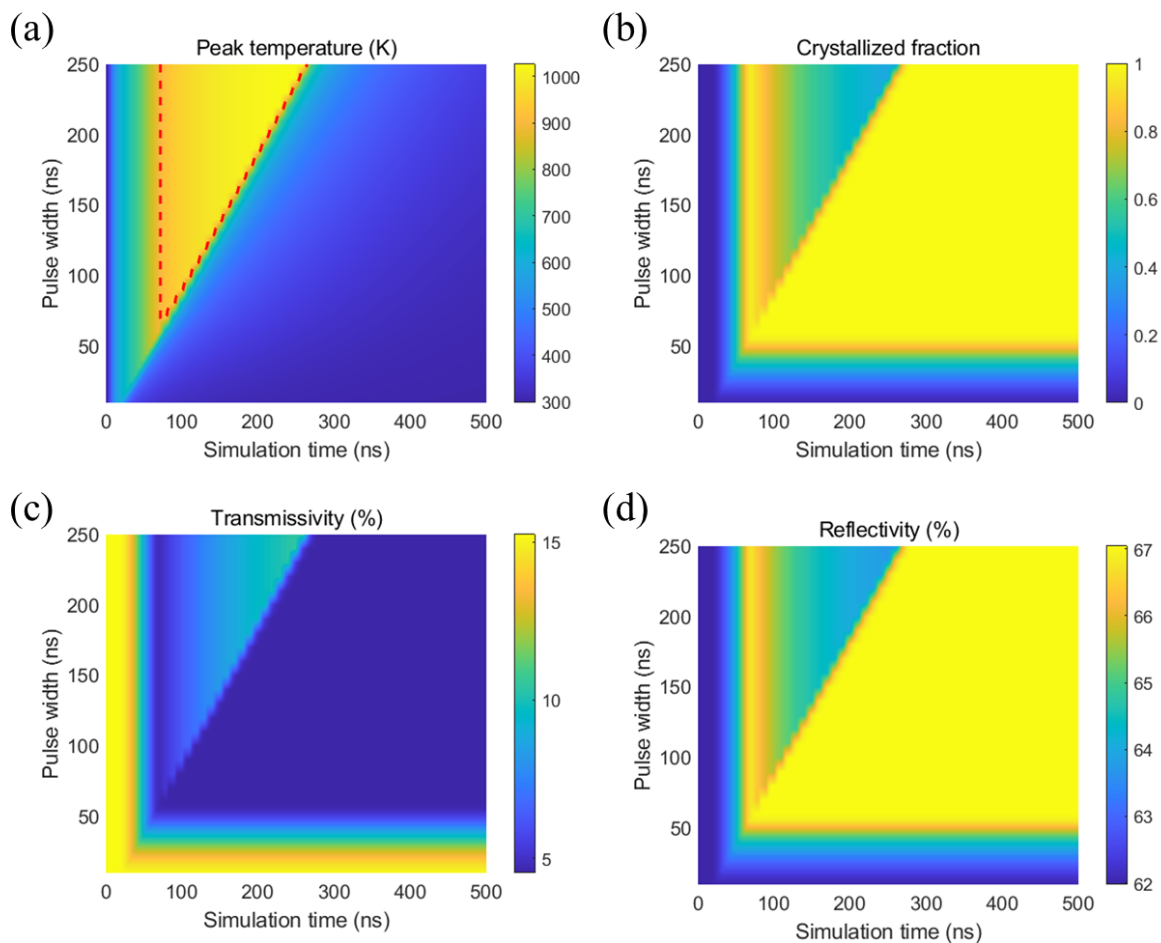


Figure S7. Transient evolution of (a) peak temperature, (b) crystallised fraction, (c) transmissivity and (d) reflectivity at different laser pulse widths.

S10. Experimental procedures.

Figure S8 shows the schematic diagram of main experimental procedures. A 50 nm-thick silicon nitride (Si_3N_4) grid was first selected as the substrate. Then a 30 nm thick $\text{Ge}_2\text{Sb}_2\text{Te}_5$ film was deposited onto the substrate in a vacuum chamber by a magnetron sputtering device.

The substrate was adhered onto a silica glass by silver glue before deposition, and then mounted onto our home-made dual-wavelength static tester to make some crystallisation marks under different pulse width and laser power. Then, the substrate was taken off from the glass and continued the transmission electron microscopy (TEM) measurement on Titan Confocal TEM.

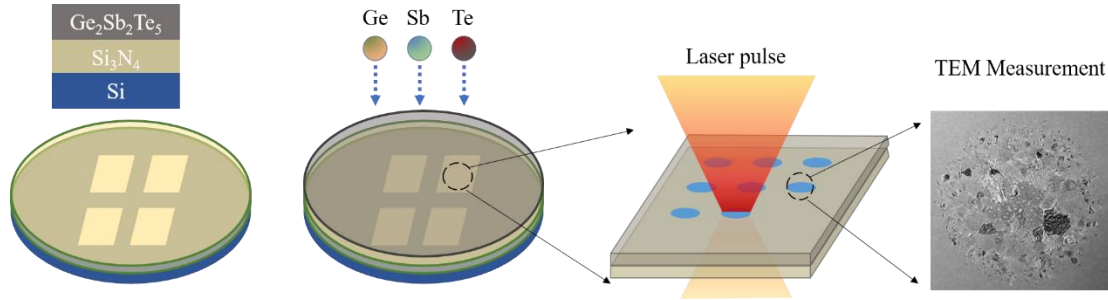


Figure S8. Experimental procedures.

S11. Measured relative transmissivity change.

Obviously, when laser power is larger than 5.5 mW, the relative transmissivity change of final state becomes much larger than background. This is due to laser ablation removing materials away from sample surface (see Figure S10).

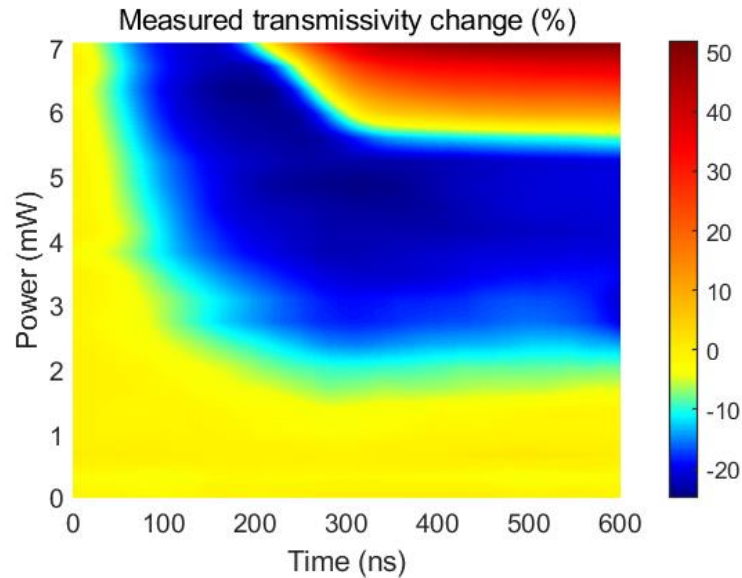


Figure S9. Evolution of measured relative transmissivity change during crystallization at a power range of 0 mW to 7.0 mW. Negative/positive value means the decrease/increase of the transmissivity.

S12. Crystallographic structure at 5.5 mW.

Figure S10 shows the crystallographic structure of the $\text{Ge}_2\text{Sb}_2\text{Te}_5$ sample after crystallisation at 5.5 mW. The center white region is caused by laser ablation due to high laser power.

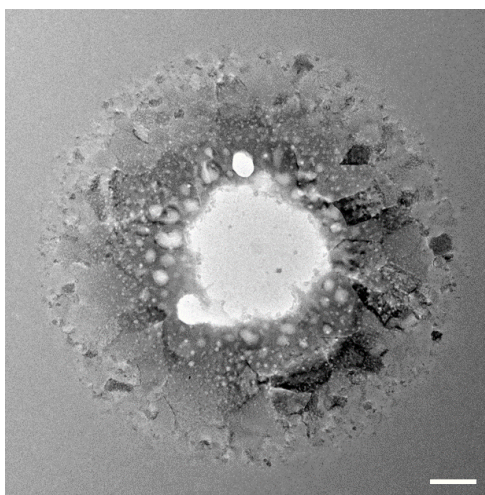


Figure S10. Crystallographic structure at 5.5 mW.

S13. Selected area electron diffraction (SAED)

To check the crystallographic structures and grain size distributions, the selected area electron diffraction (SAED) patterns were measured at the center and border of crystallisation regions, shown in Figure S11(a) and S11(b), respectively. As a reference, the SAED pattern at amorphous background was also measured, shown in Figure S11(c). Discrete dots rather than rings indicate the successful crystallisation. The irregularity of these dots shows the polycrystalline nature of the crystallised regions which contain many grains with different orientations. More dots in Figure S11(b) than Figure S11(a) imply that there are more grains with different orientations at the border than at the center for same measurement range. That is, the grain sizes at the center are larger than those at the border.

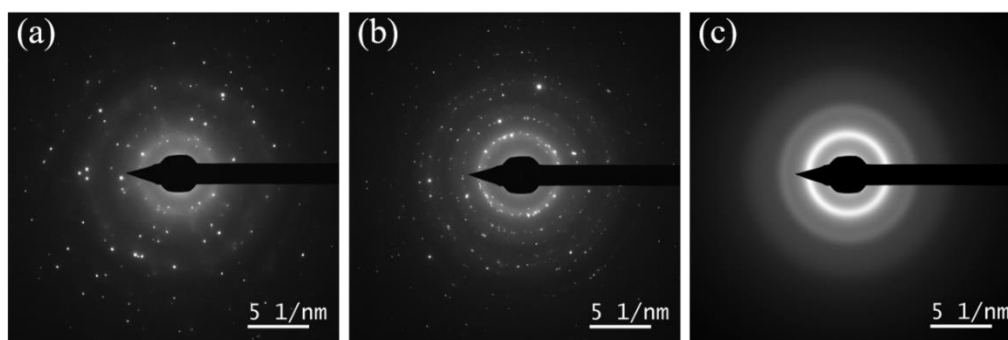


Figure S11. SAED patterns (a) at the center and (b) at the border of crystallisation region and (c) at amorphous region.

References.

- [1] A. Sebastian, M. Le Gallo and D. Krebs, Crystal growth within a phase change memory cell. *Nat. Commun.*, 2014, 5.
- [2] S. Senkader and C. D. Wright, Models for phase-change of Ge₂Sb₂Te₅ in optical and electrical memory devices. *J. Appl. Phys.*, 2004, 95: 504-511.
- [3] K. Kohary and C. D. Wright, Modelling the phase-transition in phase-change materials. *physica status solidi (b)*, 2013, 250: 944-948.
- [4] J. Tominaga, T. Shima, P. Fons, R. Simpson, M. Kuwahara, and A. Kolobov, What is the Origin of Activation Energy in Phase-Change Film? *Jpn. J. Appl. Phys.*, 2009, 48: 03A053.
- [5] T. C. Li, D. Weiling, L. Li, Z. Xilin, B. Jitendra, L. Hailong, V. S. Kandammathe, M. Libang, C. Tun, Y. Joel, and E. S. Robert. Chalcogenide active photonics. in *Proc.SPIE*. 2017.
- [6] J. C. Mauro, Y. Yue, A. J. Ellison, P. K. Gupta, and D. C. Allan, Viscosity of glass-forming liquids. *Proceedings of the National Academy of Sciences*, 2009, 106: 19780.